COMPUTATIONAL SIMULATION OF THE ATMOSPHERIC BOUNDARY LAYER USING SUB-OPTIMAL GRID RESOLUTION

A Thesis by

Matthew McKenna

Bachelor of Science, Wichita State University, 2013

Submitted to the Department of Mechanical Engineering
and the faculty of the Graduate School of
Wichita State University
in partial fulfillment of
the requirements for the degree of
Master of Science

May 2018

COMPUTATIONAL SIMULATION OF THE ATMOSPHERIC BOUNDARY LAYER USING SUB-OPTIMAL GRID RESOLUTION

The following faculty members have examined the final copy of this thesis for form and content, and recommend that it be accepted in partial fulfillment of the requirement for the degree of Master of Science with a major in Mechanical Engineering.

Ikramuddin Ahmed, Committee Chair

T.S. Ravigururajan, Committee Member

Gamal Weheba, Committee Member

DEDICATION

To my wife and children.

When I meet God, I am going to ask him two questions: Why relativity? And why turbulence? I really believe he will have an answer for the first.

- Werner Heisenberg

ACKNOWLEDGEMENTS

I would like to thank my advisor, Dr. Ikramuddin Ahmed, for many years of guidance and support. I would also like to thank my mother, Janna McKenna, for being an inspiration and for her unwavering love and support. A special thanks is due to Dr. DonHung Yeo for allowing the use of his research as a basis for my own and for his generous support. Finally, words cannot express how thankful I am to have had the support and encouragement of my wife and children throughout my educational endeavors.

ABSTRACT

This study explores simulation of turbulent atmospheric boundary layer (ABL) flow fields using reduced mesh resolution as a means for reducing time and computational requirements. A full resolution simulation is performed using previously developed flow fields, within `OpenFOAM`, in an effort to reproduce the statistical results of the original study. The reduced resolution simulation is run on a personal computer (PC) and the results are compared to the full resolution simulation as well as the original study. As previously observed, the sub-grid scale (SGS) model produces inaccurate results near the ground and a large z-component of the streamwise velocity gradient still exists at the top boundary. There is an exacerbation of these issues within the reduced resolution simulation, but the increase in variance and deviation of the streamwise velocity gradient from the log-law are aspects which particularly demonstrate the inadequacies of simulations with sub-optimal grid resolutions.

TABLE OF CONTENTS

Chapter **Page**

CHAPTER 1

THE ATMOSPHERIC BOUNDARY LAYER

The atmospheric boundary layer (ABL) is the lowest 1 km of the troposphere where wind shear produced by friction at the earth's surface is relevant. At the earth's surface, horizontal wind speed is expected to be zero and increases with vertical distance from the ground. The variation in velocity can be generalized by either the log-law profile or power-law profile [19]. However, the ABL is very complex and continually evolving, which poses many difficulties in predicting its behavior.

One of the most influential characteristics of the ABL on wind speed variation is its stability, which is typically classified as stable, neutrally stable, and unstable. This classification is determined by the temperature variation between the earth's surface and the top of the ABL, called the lapse rate (Γ). A system with no heat transfer (adiabatic) where temperature decreases approximately 1 °C per 100 m increase in height is called the dry adiabatic lapse rate (DALR) [7]

$$\Gamma_\alpha = -\left(\frac{dT}{dz}\right)_{adiabatic} \approx \frac{1\,^\circ\mathrm{C}}{100\,\mathrm{m}} \tag{1.1}$$

Air molecules near the surface become less dense, and therefore more buoyant, as they heat up. After absorbing enough radiant energy, the air molecules can overcome gravity and begin to rise. Assuming that the air molecules experience a lapse rate equal to the DALR, if the lapse rate of the atmosphere is less than the DALR ($\Gamma < \Gamma_\alpha$) then the air molecules will reach an elevation where they are cooler and more dense than the surrounding atmosphere. This will cause the air molecules to begin descending. This is a stable atmospheric condition. When the atmospheric lapse rate is greater than the DALR ($\Gamma > \Gamma_\alpha$), then the atmosphere is unstable. The atmospheric condition where the atmospheric lapse rate is equal to the DALR ($\Gamma = \Gamma_\alpha$) is called neutrally stable. In order to circumvent the additional computational complexity and overhead associated with simulating buoyancy effects, all simulations assume

a neutrally stable atmospheric condition. This assumption also allows for the omission of the energy equation from the computations, further reducing the computational overhead.

Perhaps the most complex aspect of the ABL is turbulence. Turbulence in the ABL contains a large variation in scales of motion where energy dissipates from the larger scales of motion to smaller scales of motion, and the smallest scales are destroyed by viscosity. Turbulent motion is also chaotic and seemingly random. However, these stochastic motions can be averaged to reveal a more distinguishable pattern of flow.

CHAPTER 2

TURBULENCE

Turbulence is, by its very nature, chaotic and complex. As a result, there are a wide range of strategies employed toward the analysis and mathematical description of turbulent structures. These strategies vary based on fluid properties, domain boundary conditions, and computational limitations, among many other parameters. This text will cover some of the strategies for turbulence within the scope of Newtonian incompressible fluids, constrained by a flat plate (the ground, for all practical purposes) in one dimension.

Limiting the scope of study to the motion of a Newtonian incompressible fluid, the continuity and Navier-Stokes equations can be employed, respectively:

$$\frac{\partial u_i}{\partial x_i} = 0 \tag{2.1}$$

$$\frac{Du_i}{Dt} = \frac{\partial u_i}{\partial t} + \frac{\partial u_i u_j}{\partial x_j} = -\frac{1}{\rho}\frac{\partial p}{\partial x_i} + 2\frac{\partial}{\partial x_j}\nu S_{ij} \tag{2.2}$$

where ρ is density, ν is kinematic viscosity, and S_{ij} is the strain-rate tensor

$$S_{ij} = \frac{1}{2}\left(\frac{\partial u_i}{\partial x_j} + \frac{\partial u_j}{\partial x_i}\right) \tag{2.3}$$

Assuming constant kinematic viscosity, equation (2.2) can be rearranged as

$$\frac{\partial u_i}{\partial t} + \frac{\partial u_i u_j}{\partial x_j} = -\frac{1}{\rho}\frac{\partial p}{\partial x_i} + \nu\frac{\partial u_i}{\partial x_j \partial x_j} \tag{2.4}$$

Tensor notation is utilized in the above equations, where $x_i = (x_1, x_2, x_3) = (x, y, z)$ are components of spatial position and $u_i = (u_1, u_2, u_3) = (u, v, w)$ are components of velocity. This paper will utilize this convention throughout. This includes the convention implying summation over components 1, 2, and 3 when indicies are repeated (i.e. ii, jj, or kk), unless otherwise specified.

2.1 Averaging

One method for determining flow characteristics is to solve equation (2.4) for all scales of motion at every time step. This method is called direct numerical simulation (DNS). In order to be accurate, a DNS requires mesh resolution to be smaller than Kolmogorov scale eddies and the domain must be large enough so that large scale eddies are not adversely affected by the boundary conditions. Large scale flow with high Reynolds numbers, such as atmospheric boundary layer (ABL) flow, requires computational resources that are immense even by today's standards.

Rather than characterizing fluid flow in absolute detail, another strategy is to characterize it statistically. One such method is to split turbulent flow variables into their average and fluctuating parts, often referred to as Reynolds decomposition. In this text, the convention of Tennekes and Lumley [17] will be used for Reynolds decomposition:

$$\tilde{a}(x_j, t) = A(x_j, t) + a(x_j, t) \tag{2.5}$$

where A and a are the mean and fluctuating parts, respectively, of turbulent variable $\tilde{a}$.

Each time an experiment is performed is called a realization. For $\tilde{u}_i(x_j, t; \alpha)$, there is stochastic variation in space, time, and between each realization α. Applying equation (2.5)

$$\tilde{u}_i(x_j, t) = U_i(x_j, t) + u_i(x_j, t) \tag{2.6}$$

we find the mean part to be $U_i(x_j, t)$. This is generally defined by the ensemble mean, which averages the stochastic variation in space and time among all realizations:

$$U_i(x_j, t) = \lim_{N \to \infty} \frac{1}{N} \sum_{\alpha=1}^{N} \tilde{u}_i(x_j, t; \alpha) \tag{2.7}$$

However, a more practical approach would be to take the time or spatial average within a single realization [19]. The time average at a position x, within realization n, is given by:

$$U_i^T(x_j, t, T; n) = \frac{1}{T} \int_0^T \tilde{u}_i(x_j, t + t'; n)\, dt' \tag{2.8}$$

where T is the averaging time. The turbulent flow is considered statistically stationary (or statistically stable), in time if the time average converges with the ensemble average as T increases:

$$\lim_{T\to\infty} U_i^T(x_j, t, T; n) = U_i(x_j) \tag{2.9}$$

The spatial average at time t within a single realization m, is given by:

$$U_i^L(x_j, t, L; m) = \frac{1}{L}\int_0^L \tilde{u}_i(x_j + x'_j, t; m)\, dx'_j \tag{2.10}$$

where L is the averaging distance. The turbulent flow is considered homogeneous if the spatial average converges with the ensemble average as L increases:

$$\lim_{L\to\infty} U^L(x_j, t, L; m) = U(x_j) \tag{2.11}$$

2.1.1 Stationary Processes

Typically, time average is used by experimentalists [19]. Spatial averaging is restricted by the computational domain size, which is purposefully kept at a minimum in order to minimize the required number of computations. However, a sufficient averaging time must be used in order for the time average to be acceptably close to the ensemble average. This allows for a transient period to pass and for all variable statistics characterizing the turbulence to become independent of time. The simplest method for assessing if a turbulence variable has become statistically stable is through its autocovariance

$$R(s) = \frac{1}{T}\int_0^T u_i(t)u_i(t+s)\, ds \tag{2.12}$$

where s is the time lag. Normalizing the autocovariance by the variance

$$\sigma^2 = \frac{1}{T}\int_0^T u_i(t)^2\, dt \tag{2.13}$$

gives the autocorrelation function

$$\rho(s) = \frac{R(s)}{\sigma^2} \tag{2.14}$$

where σ^2 is the variance and $\rho(s)$ is the autocorrelation function. The autocorrelation function has the properties:

$$\rho(0) = 1 \tag{2.15}$$

$$|\rho(s)| \leq 1 \tag{2.16}$$

as well as being an even function

$$\rho(s) = \rho(-s) \tag{2.17}$$

and is the correlation coefficient between the variable at time t and time $t + s$ [11]. A turbulence variable is considered to be stationary in time when the mean U, σ^2, $R(s)$, and $\rho(s)$ are independent of time. The autocorrelation function is particularly useful since it is expected to approach zero as time lag s increases. However, it is worth noting that the autocorrelation function will usually decrease more rapidly for a high-frequency process (i.e. where the integral time scale is smaller) [11].

2.1.2 Application of Time Averaging

Applying time averaging of stationary variable $\tilde{u}_i$ the mean part is defined as

$$U_i(x_j) = \frac{1}{T}\int_{t_0}^{t_0+T} \tilde{u}_i(x_j, t)\, dt = \langle \tilde{u}_i \rangle \tag{2.18}$$

where t_0 is the initial time. Having this definition and referring back to (2.6), it is plain to see that the mean part does not vary with time

$$\langle U_i \rangle = U_i \tag{2.19}$$

and is unaffected by time averaging. Applying equation (2.18) to equation (2.6) produces

$$\langle u_i \rangle = 0 \tag{2.20}$$

and demonstrates that the time average of the fluctuating part is equal to 0.

Assuming that differentiation commutes with time averaging

$$\left\langle \frac{\partial \tilde{u}_i}{\partial x_j} \right\rangle = \frac{\partial \langle \tilde{u}_i \rangle}{\partial x_j} = \frac{\partial U_i}{\partial x_j} \tag{2.21}$$

we can apply time averaging to the continuity equation (2.1):

$$\begin{aligned} \frac{\partial \langle \tilde{u}_i \rangle}{\partial x_i} &= 0 \\ \frac{\partial U_i}{\partial x_i} &= 0 \end{aligned} \tag{2.22}$$

which shows that the mean velocities are solenoidal. Applying (2.6) to equation (2.1) and subtracting equation (2.22):

$$\begin{aligned} \frac{\partial \langle \tilde{u}_i \rangle}{\partial x_i} &= \frac{\partial \langle U_i \rangle}{\partial x_i} + \frac{\partial \langle u_i \rangle}{\partial x_i} \\ \frac{\partial \langle u_i \rangle}{\partial x_i} &= 0 \end{aligned} \tag{2.23}$$

shows that the velocity fluctuations are also solenoidal [8].

The principles shown in equations (2.19) - (2.23) can be applied to equation (2.4) to produce the Reynolds averaged Navier-Stokes (RANS) equation:

$$\frac{\partial (U_i U_j)}{\partial t} + \frac{\partial \langle u_i u_j \rangle}{\partial x_j} = -\frac{1}{\rho}\frac{\partial P}{\partial x_i} + \nu \frac{\partial^2 U_i}{\partial x_j \partial x_j} \tag{2.24}$$

which reveals the Reynolds stress term $\langle u_i u_j \rangle$. Since the Reynolds stress terms are not known, there are not enough equations to solve the problem. This produces what is referred to as the "closure problem".

2.2 Mixing Length

In 1877, Joseph Boussinesq proposed that Reynolds stresses could be proportional to the mean strain-rate:

$$\tau_{ij}^R = -\rho \langle u_i u_j \rangle = \nu_t \left(\frac{\partial U_i}{\partial x_j} + \frac{\partial U_j}{\partial x_i} \right) - \frac{2}{3}\rho k \delta_{ij} \tag{2.25}$$

$$k = \frac{1}{2}\left(\langle u^2 \rangle + \langle v^2 \rangle + \langle w^2 \rangle \right) \tag{2.26}$$

where k is the turbulent kinetic energy per unit mass, ν_t is the kinematic eddy viscosity, and δ_{ij} is the Kronecker delta ($\delta_{ij} = 1$ if $i = j$ and $\delta_{ij} = 0$ if $i \neq j$). Note that the last term on the right side of equation (2.25) assumes that the normal Reynolds stress components are isotropic by allocating an equal third to each component.

Mixing length models express Reynolds stresses using algebraic formulae for eddy viscosity as a function of position. However, the underlying assumption is that the ratio between the Reynolds stresses and mean strain-rate is the same in all directions [18].

The kinematic eddy viscosity, ν_t, is the product of a turbulence length scale ℓ and turbulent velocity scale ϑ with units m^2/s. Dimensional analysis produces

$$\nu_t = C\vartheta\ell \tag{2.27}$$

where C is a dimensionless constant of proportionality. The turbulence length scale ℓ is the characteristc length of the largest eddies, which contain the majority of turbulent kinetic energy. Assuming that the turbulent kinetic energy has a strong influence on the mean flow, it may be reasonable to assume that the turbulent velocity scale is proportional to the product of the turbulent length scale and mean velocity gradient

$$\vartheta = c\ell \left| \frac{\partial U_i}{\partial x_j} \right| \tag{2.28}$$

where c is a dimensionless constant of proportionality. The absolute value ensures that the velocity scale is positive, regardless of mean velocity gradient. Substituting equation (2.28) into equation (2.27) and absorbing the constants into the mixing length, ℓ_m produces

$$\nu_t = \ell_m^2 \left| \frac{\partial U_i}{\partial x_j} \right| \tag{2.29}$$

often referred to as Prandtl's mixing length model.

2.3 Near-Wall Turbulence

Reynolds number, Re provides a ratio between the inertial and viscous scales of motion. One form of Reynolds number, which is particularly useful for wall bounded flows, is based on distance from the wall:

$$\mathrm{Re}_z = \frac{Uz}{\nu} \tag{2.30}$$

where z is the direction normal to the wall. This reveals that the flow is dominated by inertia forces when z is of the same order as the length scale, L, in the flow direction. However, Re_z

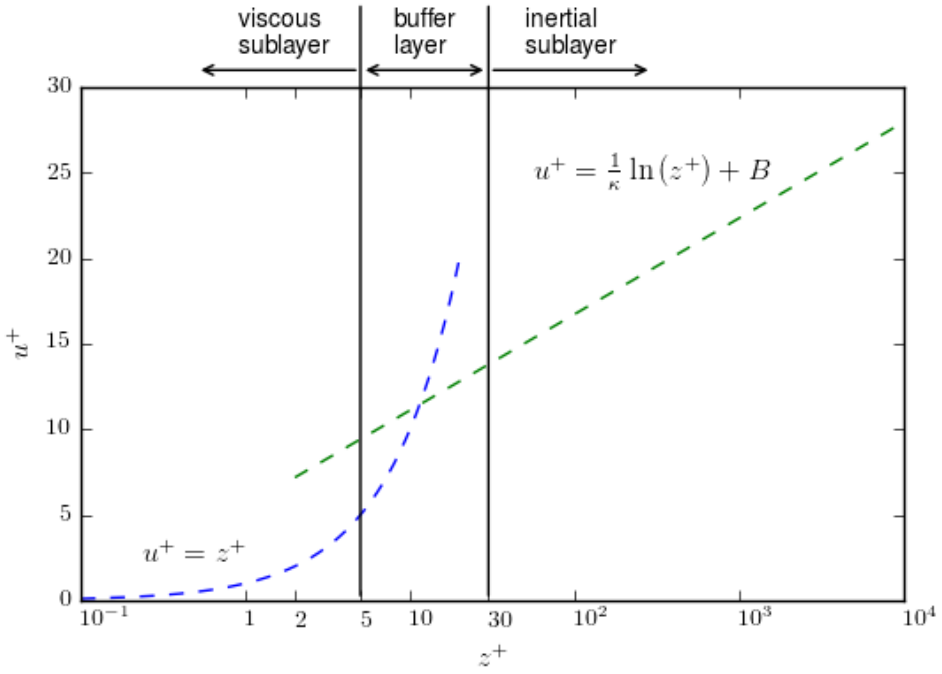

Figure 2.1: The law of the wall

approaches 0 as z approaches 0, at the wall. This means that near the wall viscous forces approach, and eventually overcome, the magnitude of the inertial forces. When this happens, the flow is dominated by viscous effects instead of free stream parameters. The mean flow becomes dependent only on distance from the wall z, fluid density ρ, fluid viscosity μ, and wall shear stress τ_w. Dimensional analysis produces

$$U = f(z, \rho, \mu, \tau_w) \tag{2.31}$$

$$u^+ = \frac{U}{u_*} = f\left(\frac{\rho u_* z}{\mu}\right) = f\left(z^+\right) \tag{2.32}$$

$$u_* = \left(\frac{\tau_w}{\rho}\right)^{1/2} \tag{2.33}$$

where u_* is the friction velocity, u^+ is nondimensional velocity, and z^+ is nondimensional wall distance. Equation (2.32) is referred to as the law of the wall [18].

Far from the wall, velocity is influenced by momentum exchange with subsequently lower fluid layers. This causes a retarding effect through the value of the wall shear stress,

but not by viscosity itself [18]. With the boundary layer thickness δ as the length scale, dimensional analysis of the mean flow produces

$$U = g(z, \delta, \rho, \tau_w) \tag{2.34}$$

$$u^+ = \frac{U}{u_*} = g\left(\frac{z}{\delta}\right) \tag{2.35}$$

The diminishing effect of the wall shear stress, with increasing distance from the wall and approaching edge of the boundary layer, can be shown by introducing a velocity deficit, $U_{\max} - U$, to form the velocity-defect law [18]:

$$\frac{U_{\max} - U}{u_*} = g\left(\frac{z}{\delta}\right) \tag{2.36}$$

Dimensional analysis of the Reynolds stress within the context of the turbulent kinetic energy budget [17] also produces equation (2.36). However, it must be noted that as $z/\delta \to 0$, in the near-wall region, δ is not the appropriate length scale and equation (2.36) is not applicable. Instead, it is used as an analogy for showing that, far from the wall, a velocity gradient occurs as effect of momentum exchange rather than directly from viscous forces.

2.3.1 The Viscous Sub-Layer

The viscous sub-layer extends from the wall to approximately $z^+ = 5$ [3, 17, 18]. In this region, the flow is dominated by viscous forces which damp out turbulence and reduce the contribution of fluctuations to the total stress [17]. Therefore, the flow is assumed to be mostly laminar with constant shear stress. This region is also very thin and the shear stress is assumed to be equal to the wall shear stress:

$$\tau(z) = \mu\left(\frac{\partial U}{\partial z}\right) \approx \tau_w \tag{2.37}$$

Integration with respect to z with the boundary condition $U = 0$ at $z = 0$ results in a relationship between the mean velocity and distance from the wall

$$U = \frac{\tau_w z}{\mu} \tag{2.38}$$

Applying equation (2.32) to equation (2.38) produces

$$u^+ = z^+ \tag{2.39}$$

2.3.2 The Inertial Sub-Layer

The inertial sub-layer is approximately in the region $30 < z^+ < 500$ where both viscosity and turbulent effects are important [18]. The first assumption is that shear stress is constant and equal to wall shear stress. The second assumption is that $\ell_m = \kappa z$, where κ is the von Karman constant. These assumptions result in the derivation of a relationship between u^+ and z^+ is described by the log-law:

$$u^+ = \frac{1}{\kappa} \ln z^+ + B \tag{2.40}$$

where $\kappa = 0.41$ and $B \approx 5.5$ for smooth walls [3, 18]. The same result can also be produced using the intermediate limit process and similarity arguments [17] for equating the velocity gradient between the inertial and viscous scales.

2.3.3 The Log-Law for a Rough Wall

The effect of roughness is negligible as long as the root mean square (rms) roughness height, z_0, is contained within the viscous sub-layer, where Reynolds stresses are suppressed. The use of a roughness Reynolds number

$$\mathrm{Re}_{z_0} = \frac{z_0 u_*}{\nu} \tag{2.41}$$

represents the ratio between the roughness height and characteristic length u_*/ν. For $\mathrm{Re}_{z_0} > 5$, turbulence increasingly becomes a result of wakes produced from the roughness and viscous forces become less relevant. This requires modification of equation (2.32):

$$u^+ = \frac{U}{u_*} = f\left(\frac{z}{z_0}, \mathrm{Re}_{z_0}\right) \tag{2.42}$$

and equation (2.40) becomes:

$$u^+ = \frac{1}{\kappa} \ln \frac{z}{z_0} + f(\mathrm{Re}_{z_0}) \tag{2.43}$$

where $f(\mathrm{Re}_{z_0})$ becomes constant as $\mathrm{Re}_{z_0} \to \infty$. Often, this term is included within z_0 in order to make $U = 0$ at $z/z_0 = 1$, below which the logarithmic profile ceases to be valid [17]. Arriving at equation (2.43) within the context of the ABL is covered in great detail by Blackadar and Tennekes [2].

CHAPTER 3

LARGE EDDY SIMULATION

3.1 The LES Framework

Large eddy simulations offer a means for focusing computing resources on the large scale motions which dominate the transfer of momentum, heat, and particulates. In contrast, nearly all of the computing resources are consumed on calculations for the small and intermediate scales of motion within DNS simulations [3]. In order to make the distinction between scales, a spatial filter is employed using a filter function:

$$\bar{\phi}(x_i, t) = \int_{-\infty}^{\infty} G(x_i, x_i', \Delta)\phi(x_i', t)\, dx_i' \tag{3.1}$$

where $\phi(x_i, t)$ is the original function, $\bar{\phi}(x_i, t)$ is the filtered function, Δ is the filter cutoff width, and $G(x_i, x_i', \Delta)$ is the filter kernel. In this section, an overbar will denote grid-scales (GS) (also known as resolved or filtered scales) and a prime will represent sub-grid scales (SGS):

$$\phi = \overline{\phi} + \phi' \tag{3.2}$$

There are three types of filtering that are most common [18]

- Top-hat filter:

$$G(x_i, x_i', \Delta) = \begin{cases} 1/\Delta^3 & |x_i - x_i'| \leq \Delta/2 \\ 0 & |x_i - x_i'| > \Delta/2 \end{cases} \tag{3.3}$$

- Gaussian filter:

$$G(x_i, x_i', \Delta) = \left(\frac{\gamma}{\pi\Delta^2}\right)^{3/2} \exp\left(-\gamma \frac{|x_i - x_i'|^2}{\Delta^2}\right) \tag{3.4}$$

$$\text{typically, } \gamma = 6$$

- Spectral cutoff filter:

$$G(x_i, x_i', \Delta) = \prod_{i=1}^{3} \frac{\sin\left[\left(x_i - x_i'\right)/\Delta\right]}{\left(x_i - x_i'\right)} \tag{3.5}$$

The top-hat filter is used in finite volume methods where the filter width, Δ, is typically equal to the grid size [4, 18]:

$$\Delta = \sqrt[3]{\Delta x \Delta y \Delta z} \tag{3.6}$$

Applying a spatial filter to equation (2.4), assuming the filter commutes with differentiation, results in the filtered momentum equation:

$$\frac{\partial \overline{u}_i}{\partial t} + \frac{\partial(\overline{u_i u_j})}{\partial x_j} = -\frac{1}{\rho}\frac{\partial \overline{p}}{\partial x_i} + \nu \frac{\partial^2 \overline{u}_i}{\partial x_j \partial x_j} \tag{3.7}$$

Since $\overline{u_i u_j} \neq \overline{u}_i \overline{u}_j$, the residual stress tensor (or sub-grid scale stress tensor) is introduced:

$$\tau_{ij} = \rho\left(\overline{u_i u_j} - \overline{u}_i \overline{u}_j\right) \tag{3.8}$$

which is similar to the Boussinesq approximation in (2.25) and results in the following filtered equation:

$$\frac{\partial \overline{u}_i}{\partial t} + \frac{\partial(\overline{u}_i \overline{u}_j)}{\partial x_j} = -\frac{1}{\rho}\frac{\partial \overline{p}}{\partial x_i} - \frac{1}{\rho}\frac{\partial \tau_{ij}}{\partial x_j} + \nu \frac{\partial^2 \overline{u}_i}{\partial x_j \partial x_j} \tag{3.9}$$

The τ_{ij} term is contains both resolved and sub-grid scale parts. However, $\tau_{ij} \to 0$ as $\Delta \to 0$ which is why it is often referred to as the SGS stress tensor. This term can be further decomposed into three separate terms:

$$\frac{\tau_{ij}}{\rho} = \overline{\left(\overline{u_i} + u_i'\right)\left(\overline{u_j} + u_j'\right)} - \overline{u}_i \overline{u}_j \tag{3.10a}$$

$$= \left(\overline{\overline{u}_i \overline{u}_j} - \overline{u}_i \overline{u}_j\right) + \left(\overline{\overline{u}_i u_j'} + \overline{u_i' \overline{u}_j}\right) + \overline{u_i' u_j'} \tag{3.10b}$$

$$= L_{ij} + C_{ij} + R_{ij} \tag{3.10c}$$

where L_{ij} is the Leonard stress term, C_{ij} is the cross-stress term, and R_{ij} is the Reynolds stress term. Leonard stresses are solely computed from the resolved velocity field and represents the interaction of resolved eddies to produce sub-grid turbulence [4,18]. The cross-stress term represents the interactions between the resolved scale and SGS eddies. The Reynolds stress term represents the convective momentum transfer of the SGS eddies, which is modeled with a SGS turbulence model [4,18]. However, the SGS stress term is typically modeled as a whole rather than as decomposed terms (3.10) [4].

3.2 Sub-Grid Scale Modeling

Since the objective of LES is to only resolve the large scales of motion, the dissipative scales are generally not resolved. The SGS model serves to provide the energy dissipation associated with the energy cascade by extracting energy from the resolved scales. One of the most popular methods for accomplishing this is through the use of an eddy-viscosity model (refer to section 2.2). By assuming that the normal stresses are isotropic and that SGS stresses are proportional to the mean rate of strain for the resolved flow, the SGS stress tensor becomes:

$$\tau_{ij}^R = 2\rho\nu_R\overline{S}_{ij} + \frac{2}{3}\rho k\delta_{ij} \tag{3.11}$$

$$k_R = \frac{1}{2}\tau_{kk}^R \tag{3.12}$$

$$\overline{S}_{ij} = \frac{1}{2}\left(\frac{\partial\overline{u}_i}{\partial x_j} + \frac{\partial\overline{u}_j}{\partial x_i}\right) \tag{3.13}$$

where ν_R is the eddy viscosity of the residual flow (or SGS viscosity), k_R is the SGS kinetic energy, $\overline{S}_{ij}$ is the resolved flow strain-rate tensor, and δ_{ij} is the kronecker delta. The isotropic part of the SGS stress tensor, $\frac{1}{3}\tau_{kk}^R\delta_{ij}$, is either modeled or expressed in the filtered pressure [4, 13].

3.2.1 The Smagorinsky Model

The Smagorinsky model was proposed in the 1960's and assumes that the smallest turbulent eddies are isotropic and immediately dissipate all energy received from the resolved scales. This model builds on Prandtl's mixing length model (equation (2.29)) and assumes that SGS viscosity can be described in terms of one length scale and one velocity scale:

$$\nu_R = (C_s\Delta)^2\,|S| \tag{3.14}$$

$$|S| = \left(2\overline{S}_{ij}\overline{S}_{ji}\right)^{1/2} \tag{3.15}$$

where C_s is the Smagorinsky constant. Suggested values for C_s are between 0.17 and 0.24 [18] based on decay rates of isotropic turbulence within the inertial subrange of the energy spectrum. However, the Smagorinsky model tends to suffer from excessive dissipation in high

shear regions [3, 4, 18]. As a result $C_s \approx 0.1$ is suggested to account for flows containing anisotropic turbulence [3, 18]. Due to the assumption of equilibrium between resolved scales and SGS scales, the Smagorinsky model becomes increasingly inaccurate where non-equilibrium conditions commonly occur. These conditions include separating and reattaching flows, boundary layers, and wall dominated domains [4].

3.2.2 One-Equation Models

Rather than making adjustments to C_s to account for non-equilibrium conditions, one-equation models use an a quantity which is more representative of the SGS velocity scale and an solve an additional transport equation to determine its distribution. Consistent with the one-equation SGS model used in this work, the square root of the SGS turbulent kinetic energy, k, will be used as the SGS velocity scale for determining eddy viscosity:

$$\nu_R = C_k \Delta k_R^{1/2} \tag{3.16}$$

$$\frac{\partial k_R}{\partial t} + \frac{\partial \left(k_R u_j\right)}{x_j} = \frac{\partial}{\partial x_j}\left[\left(\nu + \nu_R\right)\frac{\partial k_R}{\partial x_j}\right] + 2\nu_R \overline{S}_{ij}\overline{S}_{ij} - \epsilon \tag{3.17}$$

$$\epsilon = \frac{C_\epsilon k_R^{3/2}}{\Delta} \tag{3.18}$$

where ϵ represents the rate of dissipation of SGS turbulent kinetic energy. C_k and C_ϵ are constants. This is the one-equation model originally proposed by Yoshizawa [20].

While one-equation models provide a more accurate time scale, resulting from independent definition of the velocity scale [4], they still suffer from inaccuracies due to the assumption that the principle SGS stresses are isotropic and locally aligned with the strain rate tensor. This is particularly problematic near solid boundaries where the smallest scales of turbulence are anisotropic.

3.2.3 Wall Models

One method employed for increasing accuracy in the viscous sub-layer are van Driest type damping functions. These functions limit eddy viscosity by changing the mixing length so that turbulent mixing increases more slowly with increasing distance from the wall. In

the inertial sub-layer, the mixing length assumed to be $\ell_m = \kappa z$ or equivalently $\ell_m^+ = \kappa z^+$. However, this results in turbulent stress which increases as z^2:

$$\nu_t \frac{\partial U}{\partial z} = \ell_m^2 \left(\frac{\partial U}{\partial z} \right)^2 \tag{3.19}$$

The turbulent stress should increase more slowly [11], effectively damping turbulent mixing near the wall. The van Driest damping function is an exponential damping function used to provide this effect:

$$\ell_m = \kappa z \left[1 - \exp\left(\frac{-y^+}{A^+} \right) \right] \tag{3.20}$$

where A^+ is an empirical constant and is typically between 15 and 30 [4]. Specifying $A^+ = 26$ corresponds to $B = 5.3$ in equation (2.40) [5, 11].

Wall functions can also be utilized for improving accuracy in the near-wall region by approximating the wall shear stresses. Schumann [12] originally proposed an equilibrium stress model which correlates wall shear stresses with the mean streamwise velocity:

$$\tau_{xz,w} = \frac{\overline{u}(x, y, z_1)}{\langle \overline{u}(x, y, z_1) \rangle} \langle \tau_w \rangle \tag{3.21a}$$

$$\overline{w}_w = 0 \tag{3.21b}$$

$$\tau_{yz,w} = \nu_t \frac{\overline{v}(x, y, z_1)}{z_1} \tag{3.21c}$$

where subscripts $_{xz}$ and $_{yz}$ denote streamwise and spanwise directions, respectively, and z_1 is the normal distance of the first grid point (or cell center) away from the wall. This model assumes that the average wall shear stress is known *a priori* via the streamwise pressure gradient, the mean velocity at $z = z_1$ satisfies the logarithmic profile, and eddy viscosity at $z = z_1$ is constant [1, 9, 10].

The wall function used in this study is based on Schumann's and is taken from Shi and Yeo [14]:

$$\tau_{xz,w} = u_*^2 \frac{\overline{u}(x, y, z_1)}{|\mathbf{u}(x, y, z_1)|} = \left[\frac{\kappa \, |\mathbf{u}(x, y, z_1)|}{\ln(z_1/z_0)} \right]^2 \frac{\overline{u}(x, y, z_1)}{|\mathbf{u}(x, y, z_1)|} \tag{3.22a}$$

$$\tau_{yz,w} = u_*^2 \frac{\overline{v}(x, y, z_1)}{|\mathbf{u}(x, y, z_1)|} = \left[\frac{\kappa \, |\mathbf{u}(x, y, z_1)|}{\ln(z_1/z_0)} \right]^2 \frac{\overline{v}(x, y, z_1)}{|\mathbf{u}(x, y, z_1)|} \tag{3.22b}$$

where $|\mathbf{u}(x, y, z_1)| = (\langle u(x, y, z_1)\rangle^2 + \langle v(x, y, z_1)\rangle^2)^{1/2}$ is the magnitude of the horizontally averaged velocities at $z = z_1$ and angled brackets, $\langle\cdot\rangle$, represent horizontally averaged quantities. Rather than utilize a prescribed average wall shear stress, this variation assumes the mean streamwise velocity satisfies the logarithmic profile in order to obtain u_* from the horizontally averaged velocities at each time step.

CHAPTER 4

ATMOSPHERIC BOUNDARY LAYER SIMULATION

Simulations of atmospheric boundary layer (ABL) turbulence have become more widely available due to the availability of open source software, such as OpenFOAM. The use of large eddy simulations (LES) also require less computational resources than direct numerical simulations (DNS). However, high-performance computing resources are still required for domain sizes and Reynolds numbers representative of the ABL. This study examines the implications of using a reduced mesh resolution, reasonably sized for a modern personal computer (PC). Flow fields were provided from a previous LES of model-scale turbulent ABL flow [13]. A simulation will be conducted using those flow fields, henceforth referred to as the "fine resolution" simulation, and will be used to provide a baseline for the mean velocity profile, velocity variances and Reynolds stresses. The examined case is identical, with the exception of having a 40% reduction in grid resolution and will be referred to as the "coarse resolution" simulation.

4.1 Setup

The computational domain is $L_x \times L_y \times L_z = 2\,\mathrm{m} \times 1\,\mathrm{m} \times 1\,\mathrm{m}$, where L_x, L_y, and L_z are lengths in the streamwise, spanwise, and vertical directions, respectively. The mean velocity at the top of the domain, U_{ref}, is assumed to be 10 m/s. A kinematic viscosity of $\nu = 1.455 \times 10^{-5}\,\mathrm{m}^2/\mathrm{s}$ is used to match that of air at sea level and 15 °C. Assuming that the von Karman constant is $\kappa = 0.41$ and that the surface roughness is $z_0 = 0.00003\,\mathrm{m}$, the friction velocity is estimated using the logarithmic velocity profile

$$u_* = \frac{\kappa U_{\mathrm{ref}}}{\ln(L_z/z_0)} = 0.394\,\mathrm{m/s} \tag{4.1}$$

An `OpenFOAM` utility called `blockMesh` is used to produce a mesh with uniform cells in all directions. The full resolution mesh consists of $N_x \times N_y \times N_z = 200 \times 100 \times 100 = 2$ million cells and the reduced resolution mesh consists of $N_x \times N_y \times N_z = 120 \times 60 \times 60 = 432,000$ cells.

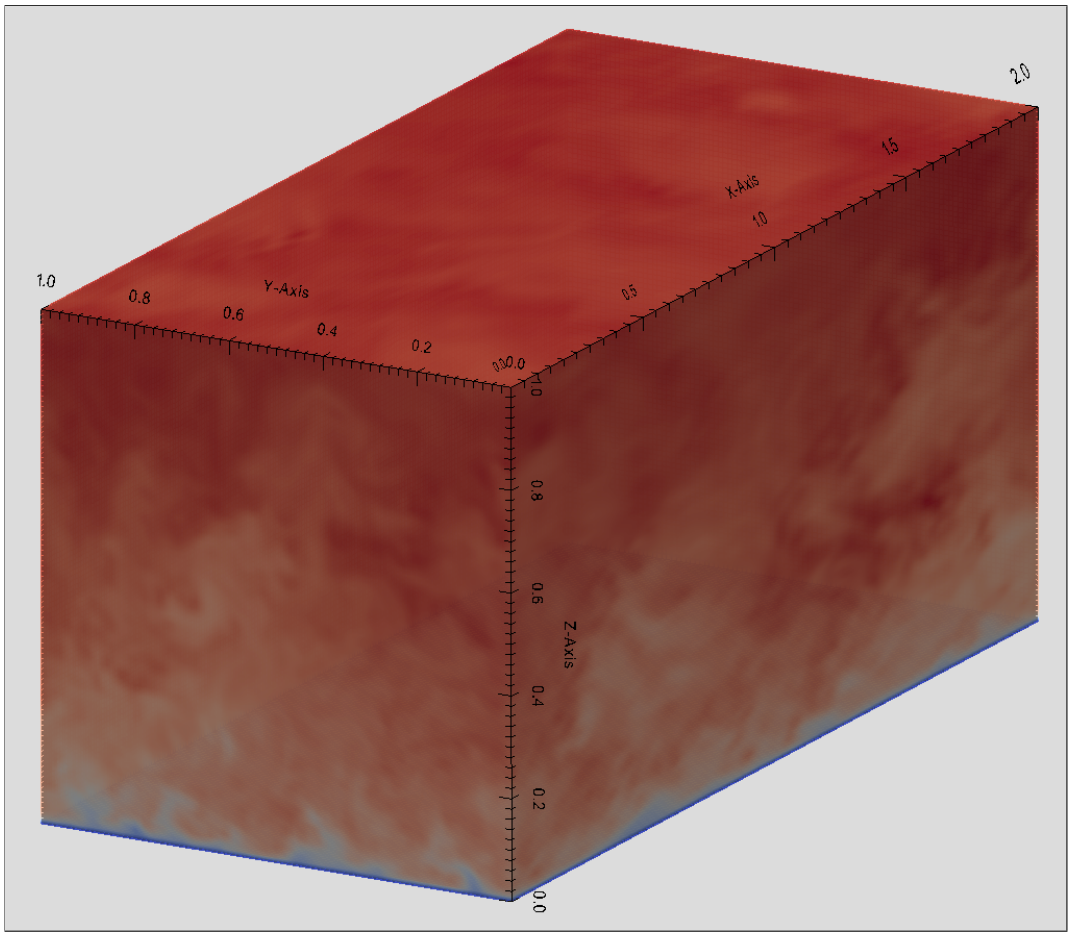

Figure 4.1: Simulation domain

Cyclic boundary conditions were used in the streamwise and spanwise directions. A no-slip condition was imposed at the ground and a slip condition at the top boundary. Zero-gradient pressure boundary conditions were imposed at the ground and at the top.

The fine resolution simulation was performed at the Wichita State University (WSU) High Performance Computing Center, utilizing 128 processors. The coarse resolution simulation was performed using a PC with 16 GB of RAM and an AMD FS-8350, utilizing 6 of the 8 cores. All computations were performed using `OpenFOAM` (version 3.0.0 at HiPeCC, and version 3.0.x on the PC). The solver used was based on the `pimpleFoam` solver, which combines the pressure-implicit split operator (PISO) and semi-implicit method for pressure-linked equations (SIMPLE) algorithms. The pressure gradient was held constant ($dp/dx = -0.1550\,\mathrm{m/s^2}$) by adding an external force, F, to the streamwise component of the Navier-Stokes equation. Time discretization was performed using the Crank-Nicolson scheme with an off-centering coefficient of 0.9 and time steps were fixed at $\Delta t = 0.00025\,\mathrm{s}$. The sub-grid scale (SGS) model used was the `kEqn` model within `OpenFOAM`, which is based off Yoshizawas one-equation turbulent energy model (refer to equation (3.17)) [4]. Constants C_k and C_ϵ were set to be 0.094 and 1.048, respectively. A wall function origially proposed by Schumann [12] is also used, and is shown in equation (3.22).

Each simulation was run for 300 flow-through times ($t_L = L_x/u_{\mathrm{ref}}$). Assuming that the turbulence was statistically stationary, mean-flow quantities were obtained along constant z planes during runtime. Temporal averaging was conducted during post-processing using data written every 5 flow-through times. Velocity values were taken at the domain center every time step for the last 100 flow-through times.

4.2 Results

Figure 4.2 shows the instantaneous velocity values taken at the domain center during the final 8000 time steps of simulation. After finding the time average of each velocity component the autocorrelation function (refer to equation (2.14)) for each component was

found using a brute-force method for finding the autocovariance:

$$R(s) = \frac{1}{N} \sum_{t=1}^{N-s} u(t)u(t+s) \tag{4.2}$$

where s is the time lag. Alternatively, the same result can be found by using the Wiener-Khinchin Theorem:

$$R(s) = \mathcal{F}_\nu \left[u_\nu(t) u_\nu^*(t) \right](s) \tag{4.3}$$

where $\mathcal{F}_\nu$ is the inverse Fourier transform operation, the subscript $_\nu$ indicates the Fourier transform, and the superscript * indicates the complex conjugate. As shown in Figure 4.3, the autocorrelation function diminishes as time lag increases. However, the autocorrelation function does not completely converge to zero. In order to investigate the statistical stability, a moving average was plotted in Figure 4.4. The autocorrelation function and moving average plots show evidence that both simulations are close, but have not quite, become statistically stationary.

Since this study is focused on horizontally homogeneous turbulent variables, the angled bracket notation, $\langle \cdot \rangle$, will be used to represent averaging in time and along horizontal planes:

$$\langle \phi(z) \rangle = \frac{1}{T} \frac{1}{L_x} \frac{1}{L_y} \int_0^T \int_0^{L_y} \int_0^{L_x} \phi(x, y, z, t)\, dx\, dy\, dt \tag{4.4}$$

The mean velocity follows the theoretical log-law profile given by

$$\langle u \rangle = \frac{u_*}{\kappa} \ln \left(\frac{z}{z_0} \right) \tag{4.5}$$

within a maximum error of about 12.3% for the fine mesh simulation and 17.2% for the coarse mesh simulation (Figure 4.5). In both simulations the largest error occurs at the top of the domain and overshooting is present [4,13,14] near the ground boundary. This overshooting is common in wall bounded LES's and is usually attributed to inaccuracies in the SGS model. However, the large deviation at the top boundary is not commonly mentioned [13, 14] and is attributed to a large z-component of the velocity gradient.

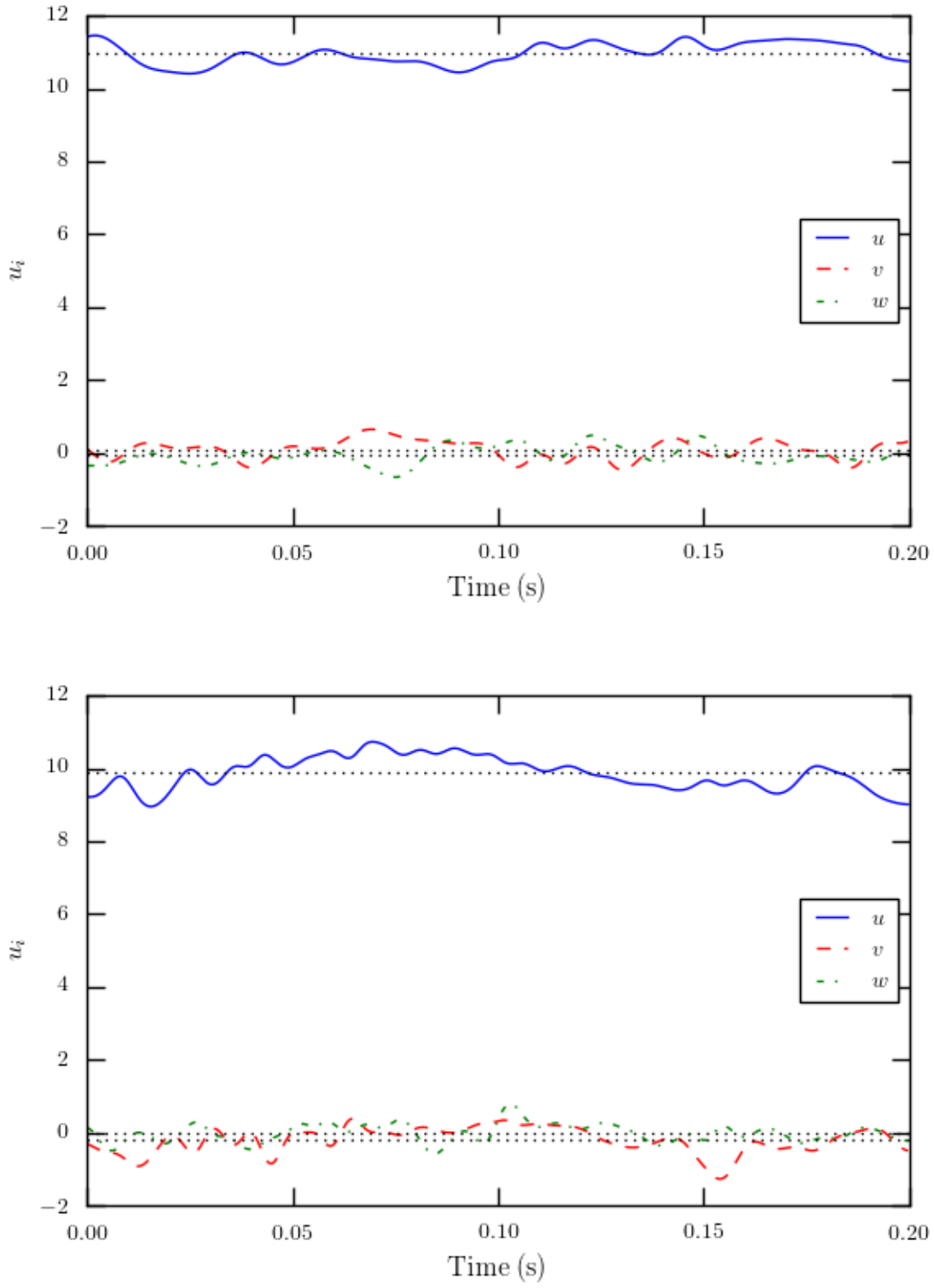

Figure 4.2: Instantaneous velocity component values, for the coarse (top) and fine (bottom) resolution simulations, from probe data over 800 time steps. Mean component values are represented with horizontal dotted lines.

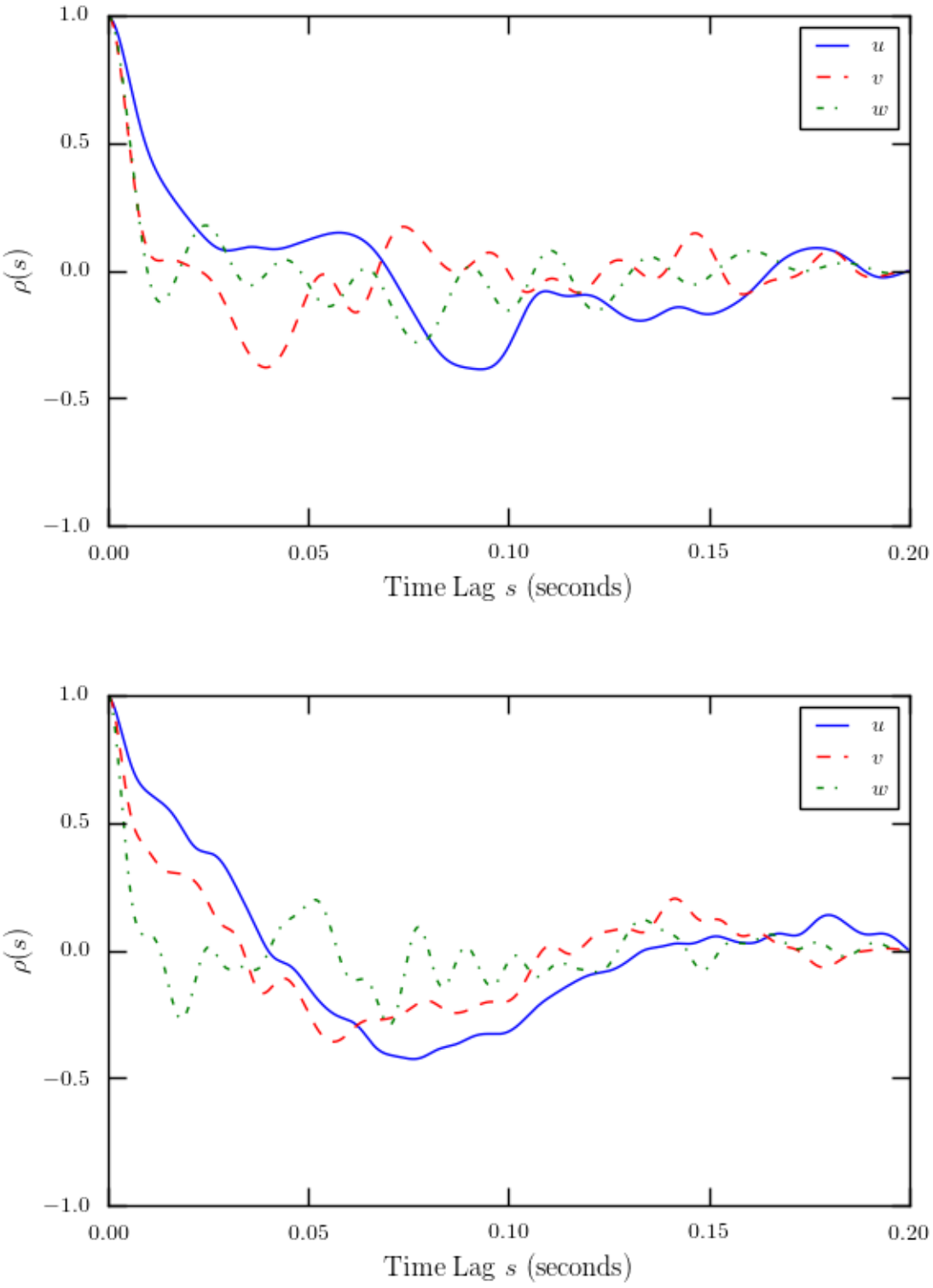

Figure 4.3: Velocity component autocorrelation, for the coarse (top) and fine (bottom) resolution simulations, produced using the summation method and probe values over 800 time steps.

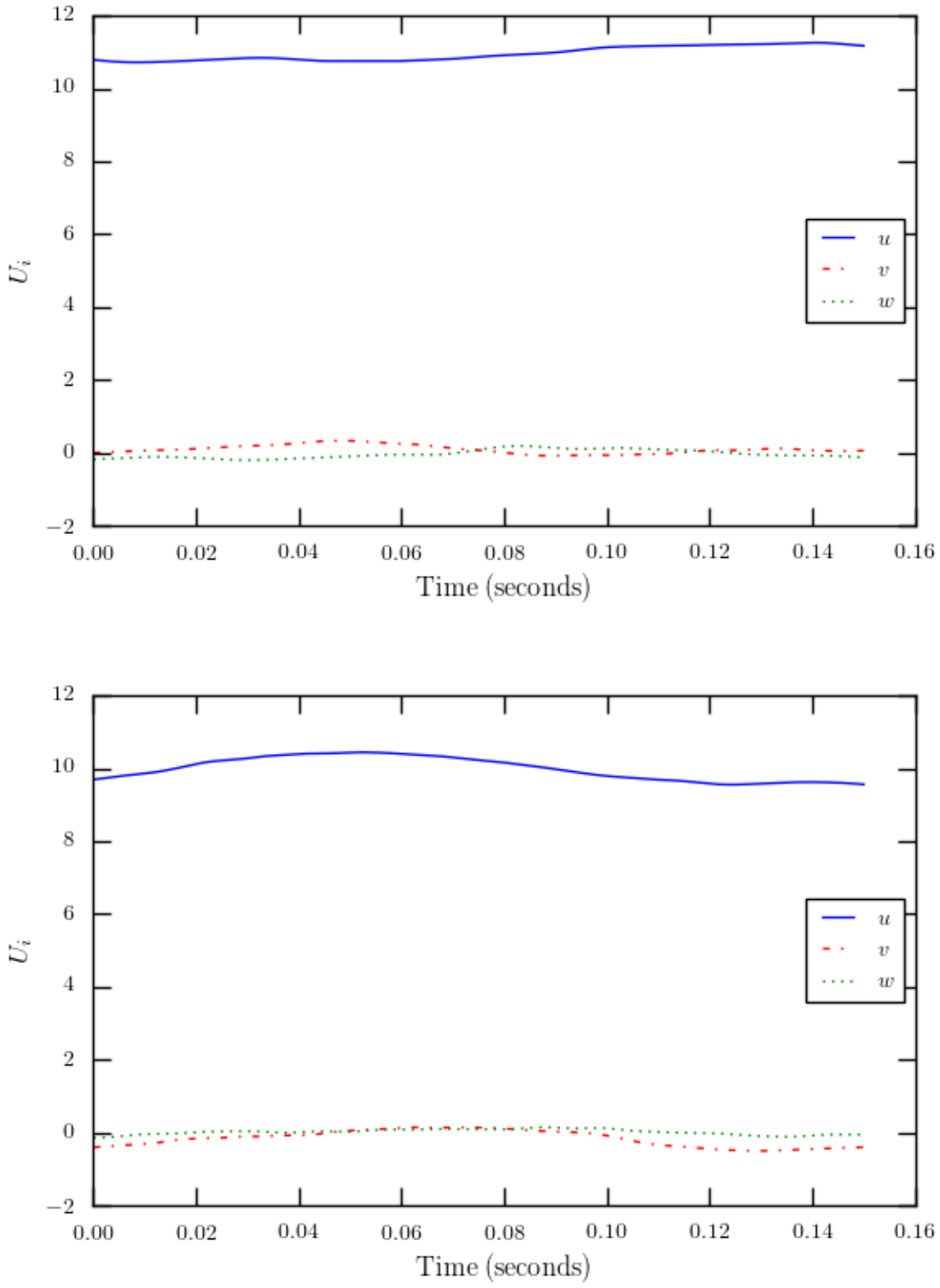

Figure 4.4: Moving average for velocity within the coarse (top) and fine (bottom) resolution simulations, produced using a 200 time step (0.05 second) window size and probe values over 800 time steps.

The nondimensional mean velocity gradient term

$$\Phi(z) = \frac{\kappa z}{u_*}\frac{d\langle u\rangle}{dz} \tag{4.6}$$

is equal to unity for the log-law profile. Similar to the results of Shi and Yeo [13], the large deviations occurring at the top and bottom boundaries are present in both simulations (Figure 4.5). However, also present in both simulations is a large deviation near $z/H = 0.6$ which does not match the results of Shi and Yeo. This deviation is more pronounced in the coarse simulation.

The velocity variances agree well with the results of Shi and Yeo [13], with the coarse simulation streamwise variance deviating from the theoretical profiles below $z/H = 0.4$ (Figure 4.6). The profiles of the mean stresses also agree well with Shi and Yeo [13], with the coarse simulation deviating from the theoretical profiles within a larger distance from the ground.

Figure 4.8 shows the nondimensional power spectra nS_u/u_*^2 for the both simulations as a function of nondimensional frequency $nz/\langle u\rangle$, where n is frequency, S_u is the power spectrum, and u_* is the expected friction velocity from equation (4.1). The provided analytical expressions are modified Kaimal expressions from [15]:

$$\frac{nS_u}{u_*^2} = \frac{200f}{(1+50f)^{5/3}} \tag{4.7}$$

$$\frac{nS_v}{u_*^2} = \frac{15f}{(1+9.5f)^{5/3}} \tag{4.8}$$

$$\frac{nS_w}{u_*^2} = \frac{15f}{(1+10f^{5/3}} \tag{4.9}$$

$$\tag{4.10}$$

for the streamwise, spanwise, and vertical components of neutrally stable flows within the inertial sub-layer of the ABL [14]. Unlike Shi and Yeo [13, 14], instantaneous values were taken from the domain center ($z = 0.5$). Similar to Shi and Yeo [13], the frequencies with the greatest spectral energy follow the analytical expressions. However, there is a lack of points at the lower frequencies, suggesting that more probing is necessary for a clearer depiction of the power spectral density.

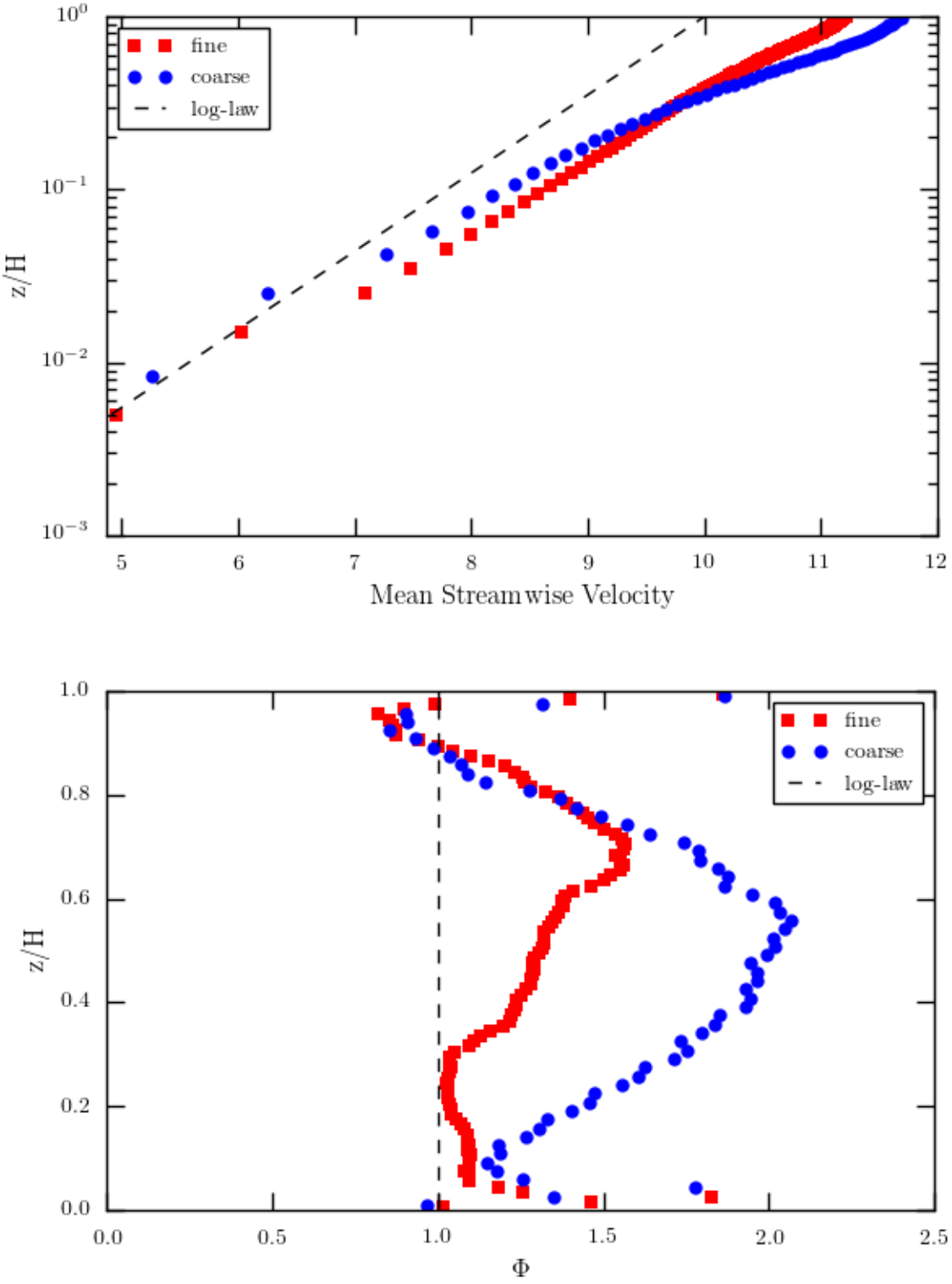

Figure 4.5: Mean streamwise velocity vertical profiles (top) for the fine and coarse simulations. Nondimensional mean velocity gradient (bottom), Φ, for the fine and coarse simulations. Dashed lines are the theoretical log-law profiles.

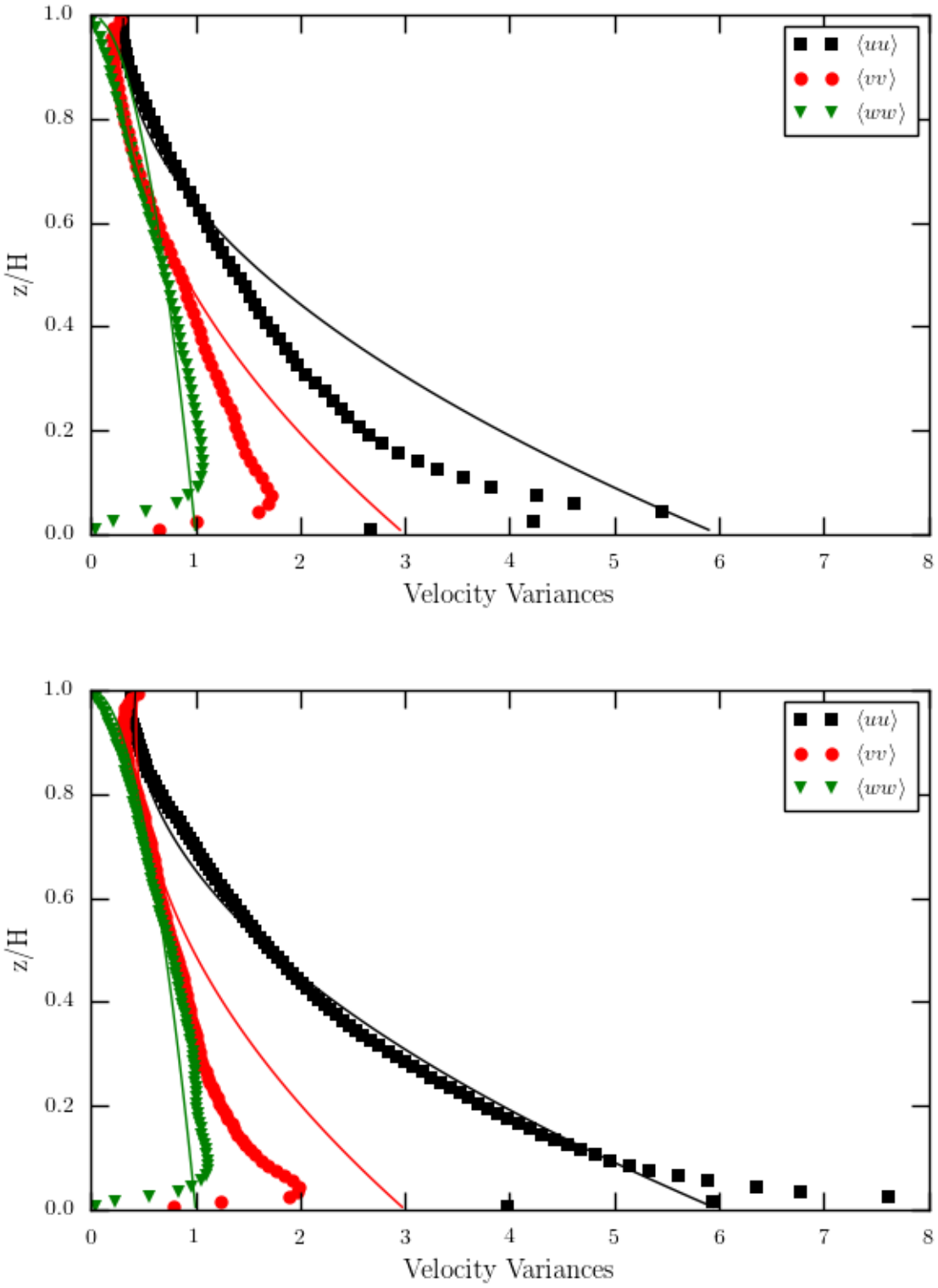

Figure 4.6: Vertical profiles of the normalized velocity variances for the coarse (top) and fine (bottom) resolution simulations. Solid lines are analytical expressions from Stull [16].

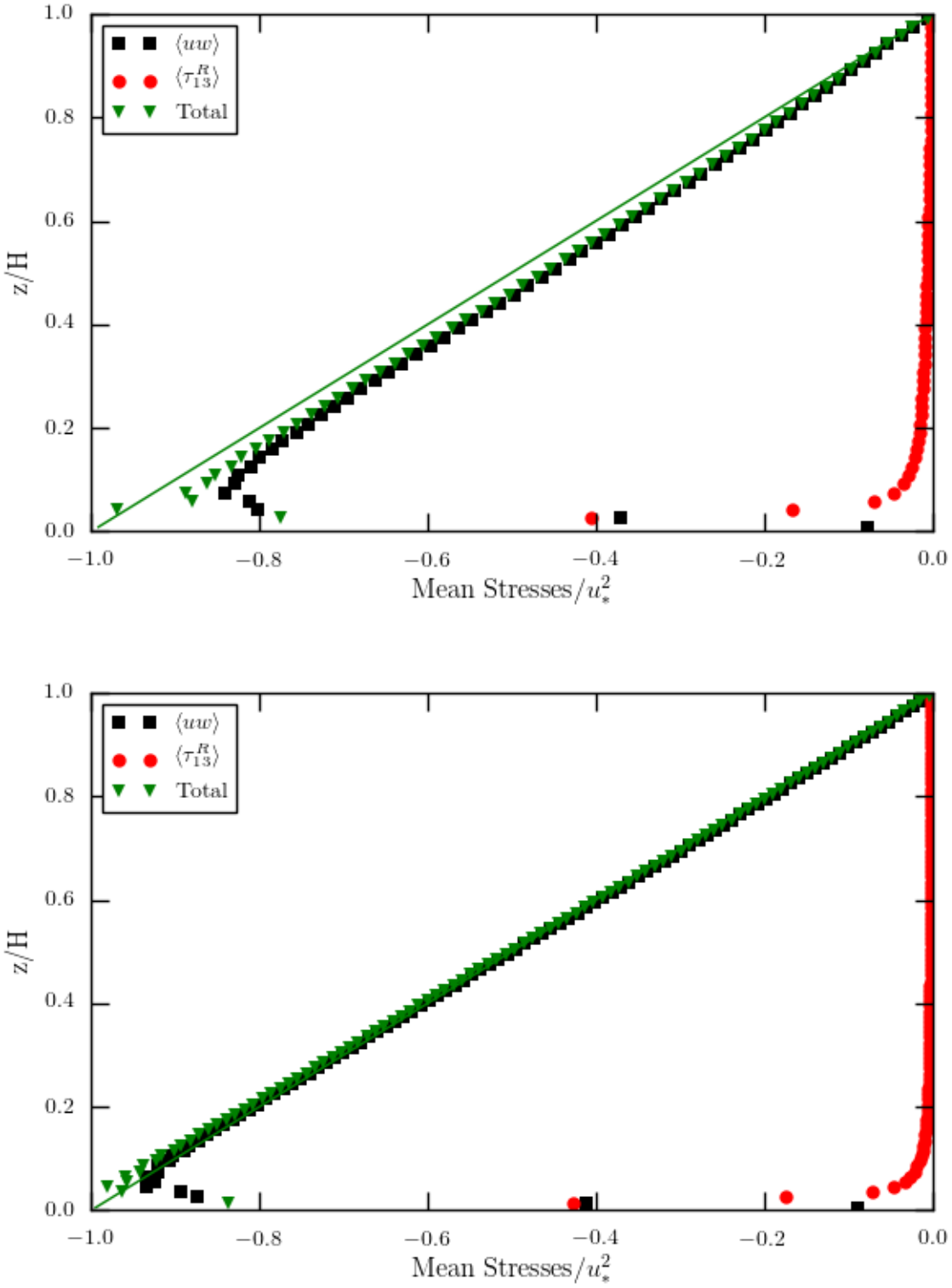

Figure 4.7: Reynolds stresses for the coarse (top) and fine (bottom) resolution simulations.

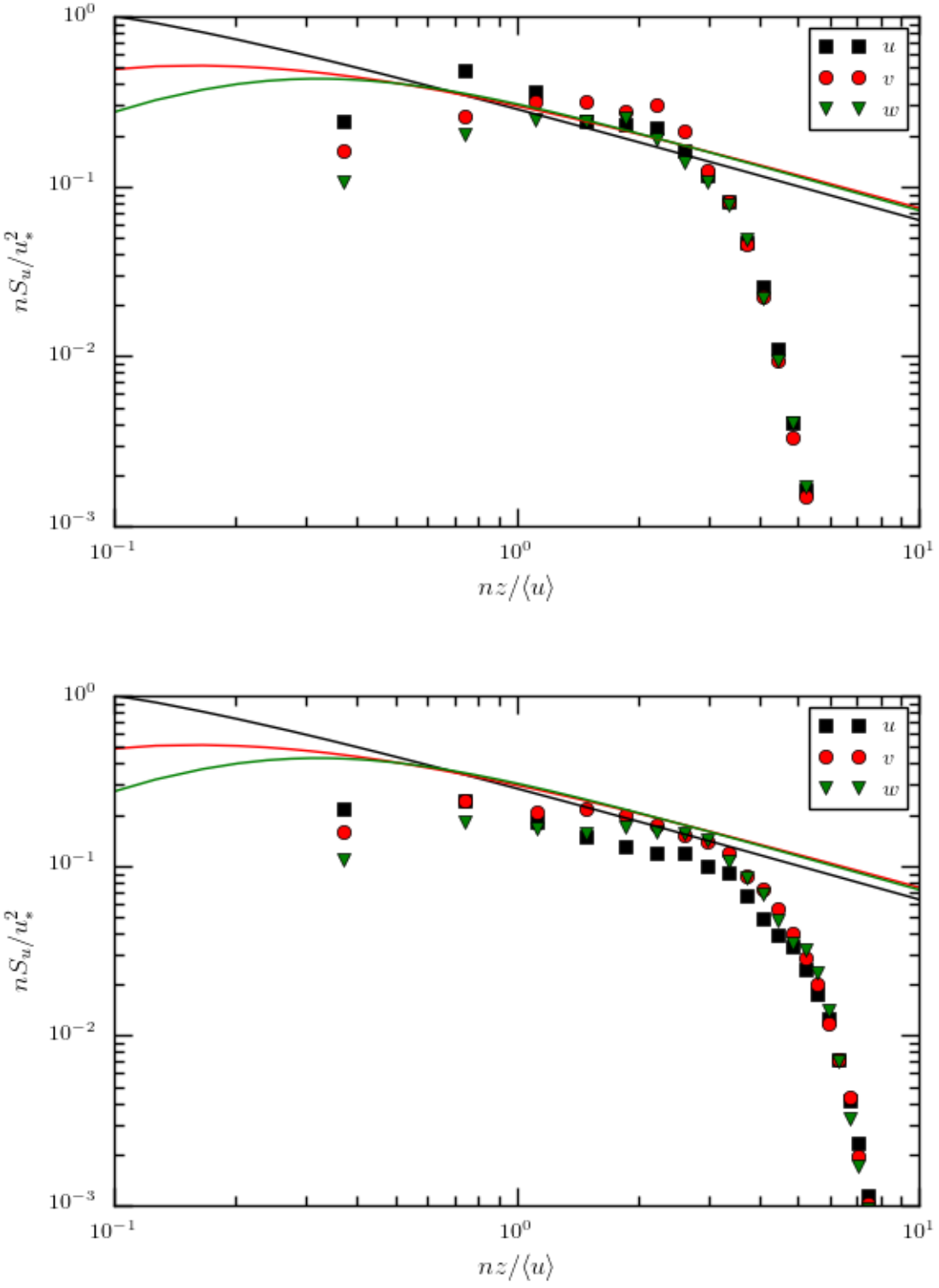

Figure 4.8: Nondimensional power spectrum for the coarse (top) and fine (bottom) resolution simulations. Solid lines are modified Kaimal expressions from [15].

4.3 Discussion

Two simulations were produced based off the results of Shi and Yeo [13]. The simulation with an identical mesh resolution was used to reproduce the results. The simulation with a 40% reduction in mesh resolution was used to produce results with PC-scale computational resources. The simulation with the fine resolution mesh produced results similar to those of Shi and Yeo [13]. However, the deviation of the mean velocity gradient from the log-law around $z/H = 0.6$ is larger than expected. This is likely due to insufficient averaging time, which was only 30% of that used by Shi and Yeo. While 300 flow-through times were simulated, it is possible that the simulation had not become statistically steady, as shown by the autocorrelation function and moving average plots. Further investigation into required simulation time to reach statistical steadiness would be beneficial for ensuring efficient use of computational resources.

As expected, the simulation with the coarse resolution mesh produced results with greater deviations from the theoretical values. One of the major drawbacks of eddy-viscosity models is the assumption that the unresolved scales of motion are isotropic. While this assumption may be sufficient for well resolved LES [4], the coarse mesh utilized in the coarse simulation is likely to be applying this assumption to significant scales of anisotropic motion. This is especially problematic in near-wall regions where flow is predominantly anisotropic. Further study is needed to determine if this is the root cause of the large mean velocity gradient near the top boundary, as well. Another possibility to consider is the potential degradation of results by the wall model. Fureby et. al. [6] found that the use of wall models or damping functions were counterproductive in improving SGS shear stress anisotropy.

REFERENCES

LIST OF REFERENCES

[1] Elias Balaras, Carlo Benocci, and Ugo Piomelli. Two-layer approximate boundary conditions for large-eddy simulations. *AIAA Journal*, 34(6):1111–1119, 1996.

[2] A. K. Blackadar and H. Tennekes. Asymptotic similarity in neutral barotropic planetary boundary layers. *Journal of the Atmospheric Sciences*, 25:1015–1020, 1968.

[3] Peter A. Davidson. *Turbulence: An Introduction for Scientists and Engineers*. Oxford University Press, New York, NY, 2nd edition, 2015.

[4] Eugene de Villers. *"The Potential of Large Eddy Simulation for the Modeling of Wall Bounded Flows"*. PhD thesis, Imperial College of Science, Technology and Medicine, 2006.

[5] P.A. Durbin and B.A. Petterson Reif. *Statistical Theory and Modeling for Turbulent Flows*. John Wiley & Sons, Chirchester, UK, 2nd edition, 2011.

[6] C. Fureby, A.D. Gosman, G. Tabor, and H.G. Weller. Large eddy simulation of turbulent channel flows. *Turbulent Shear Flows*, 11:28–13, 1997.

[7] J.F. Manwell, J.G. McGowan, and A.L. Rogers. *Wind Energy Explained: Theory, Design and Application*. John Wiley & Sons, Chirchester, UK, 2nd edition, 2009.

[8] Ronald L. Panton. *Incompressible Flow*. John Wiley & Sons, Hoboken, NJ, 4th edition, 2013.

[9] Ugo Piomelli and Elias Balaras. Wall-layer models for large-eddy simulations. *Annual Review of Fluid Mechanics*, 34:349–374, 2002.

[10] Ugo Piomelli, Joel Ferziger, Parviz Moin, and John Kim. New approximate boundary conditions for large eddy simulations of wall-bounded flows. *Physics of Fluids*, 1(6):1061–1068, 1989.

[11] Stephen B. Pope. *Turbulent Flows*. Cambridge University Press, Cambridge, UK, 2000.

[12] U. Schumann. Subgrid scale model for finite difference simulations of turbulent flows in plane channels and annuli. *Journal of Computational Physics*, 18:376–404, 1975.

[13] Liang Shi and DongHun Yeo. "Large Eddy Simulations of Model-Scale Turbulent Atmospheric Boundary Layer Flows". *Journal of Engineering Mechanics*, 143(9).

[14] Liang Shi and DongHun Yeo. "OpenFOAM Large-Eddy Simulations of Atmospheric Boundary Layer Turbulence for Wind Engineering Applications". Technical Report 1944, NIST, 2016. [Accessed March 2017].

LIST OF REFERENCES (continued)

[15] Emiu Simiu and Robert H. Scanlan. *Wind Effects on Structures: Fundamentals and Applications to Design*. John Wiley & Sons, New York, NY, 3rd edition, 1996.

[16] Roland B. Stull. *An Introduction to Boundary Layer Meteorology*. Kluwer Academic Publishers, Norwell, MA, 2nd edition, 1988.

[17] Henk Tennekes and John L. Lumley. *A First Course in Turbulence*. MIT Press, Cambridge, MA, 1972.

[18] H.K. Versteeg and W. Malalasekera. *An Introduction to Computational Fluid Dynamics: The Finite Volume Method*. Pearson Education Limited, Essex, England, 2nd edition, 2007.

[19] John C. Wyngaard. *Turbulence in the Atmosphere*. Cambridge University Press, Cambridge, UK, 2010.

[20] Akira Yoshizawa. Statistical theory for compressible turbulent shear flows, with the application to subgrid modeling. *Physics of Fluids*, 29(7):2152–2164, 1986.